

Label-Free Histology and Evaluation of Human Pancreatic Cancer with Coherent Nonlinear Optical Microscopy

Lili Zhang,[○] Xiang Zou,[○] Jing Huang,[○] Jie Fan, Xiangjie Sun, Bohan Zhang, Bin Zheng, Chongyuan Guo, Deliang Fu, Lie Yao,^{*} and Minbiao Ji^{*}



Cite This: *Anal. Chem.* 2021, 93, 15550–15558



Read Online

ACCESS |



Metrics & More

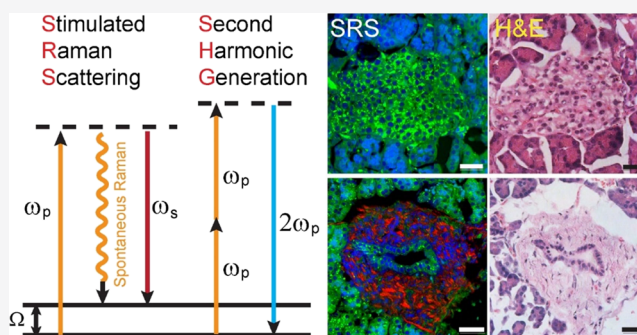


Article Recommendations



Supporting Information

ABSTRACT: Surgeries achieving maximal tumor resection remain the major effective treatment of pancreatic cancer. Rapid and precise intraoperative diagnosis of pancreatic tissues is critical for optimum surgical outcomes but is challenging for the current staining-based histological methods. We demonstrated that label-free coherent nonlinear optical microscopy with combined stimulated Raman scattering (SRS) and second harmonic generation (SHG) could reveal key diagnostic features of both normal and cancerous human pancreatic tissues. Adjacent pairs of tissue sections from resection margins of 37 patients were imaged by SRS and hematoxylin and eosin staining for direct comparison, demonstrating high diagnostic concordance (Cohen's kappa, $\kappa > 0.97$) between them. Fresh unprocessed tissues showed well-preserved histoarchitectures including pancreatic ducts, islets, acini, and nerves. Moreover, the area ratios of collagen fibers were analyzed and found to correlate with the drainage pancreatic amylase level (odds ratio = 28.0, $p = 0.0017$). Our results indicated that SRS/SHG histology provides potential for rapid intraoperative diagnosis of pancreatic cancer as well as a predictive value of postoperative pancreatic fistula.



INTRODUCTION

Pancreatic cancer has a high degree of malignancy with poor prognosis. About 80% of patients are with locally advanced or metastatic lesions, and the 5-year survival rate is about 10% in the United States.¹ Even patients who undergo surgical resections have more than 80% recurrence within 3 years.² However, radical surgery is still the only way for patients with pancreatic cancer to achieve long-term survival. Complete removal of tumor tissues (R0 resection) has been shown to remarkably improve the survival rates and provide more conservative treatment results.³ In contrast, surgeries that do not reach R0 resection have the risks of postoperative residual pancreatic tumor recurrence and peripheral metastasis, which are the most direct factors affecting prognosis. Therefore, rapid histological evaluation of surgical margins to ensure R0 resection remains a critical challenge during pancreatic operation.

In addition, pancreatic surgeons have long been plagued by pancreatic fistula, which is induced by intraoperative tissue damage leading to the leakage of pancreatic juice and enzymatic fluids that in turn invade the surrounding tissues, resulting in a vicious circle of growing extent of pancreatic fistula.⁴ It is reported that the incidence of pancreatic fistula could reach as high as 3~45% and is closely related to prognosis.⁵ Patients with postoperative pancreatic fistula tend to have increased pancreatic fat and decreased pancreatic

fibrosis, blood vessel density, and duct size.⁶ However, no significant differences are found between methods of pancreatoenteric anastomosis in terms of the occurrence of postoperative pancreatic fistula. Therefore, an imaging technique capable of quantifying tissue textures such as collagen fibrosis may provide a means to monitor the quality of anastomosis and decrease the incidence of pancreatic fistula.⁷

At present, the most commonly used method for detecting intraoperative tissue histology is intraoperative frozen hematoxylin and eosin (H&E) staining. However, it may suffer from a few drawbacks: first, tissue preparations including freezing, sectioning, and staining usually take more than half an hour; second, large amount of tissue is needed for frozen H&E staining; and lastly, the invasive processes prevent the tissues from being reused after histological inspection for additional evaluations. Therefore, there is an urgent need in the clinic for imaging techniques that take shorter time, require fewer tissues, and are noninvasive so that tissues can be repeatedly

Received: September 6, 2021

Accepted: November 1, 2021

Published: November 9, 2021



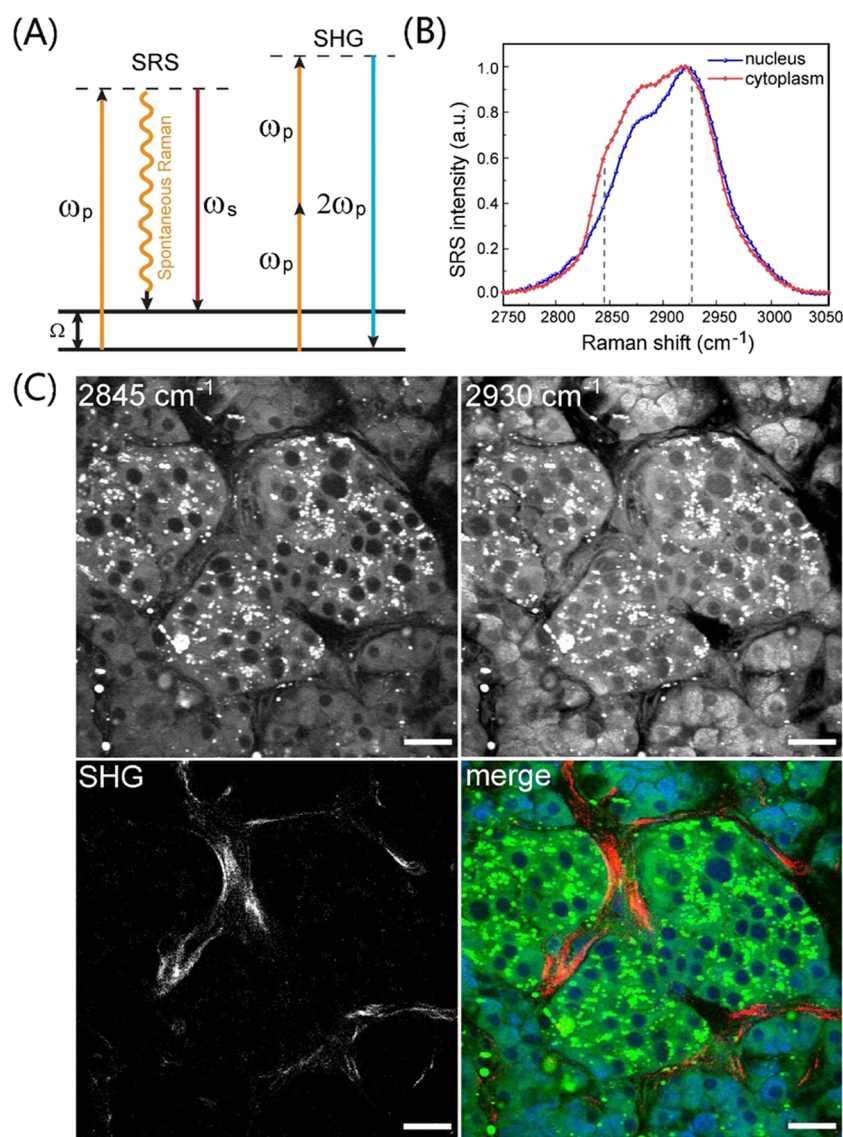


Figure 1. Experimental design. (A) Energy diagram of SRS and SHG processes. (B) SRS spectra of lipid droplets and cell nucleus in pancreatic tissues. (C) Raw SRS images of a normal pancreatic islet taken at 2845 and 2930 cm^{-1} as well as the SHG image and the composite three-color image. Green: lipids; blue: protein; and red: collagen fibers. Scale bar: 20 μm .

detected and even in vivo detection is possible to guide the R0 resection during surgery.

Advances in optical imaging techniques have revolutionized our ability to study tissue histopathology. Traditional optical microscopies such as bright field and fluorescence microscopy have played large roles in cellular and tissue imaging, but they usually require the use of exogenous labels that often perturb the system of interest and involve complex sample preparations. Autofluorescence offers certain molecular contrast, but the number of endogenous fluorophores is limited.⁸ Vibrational spectroscopy-based imaging techniques including infrared (IR) absorption and Raman scattering offer superb intrinsic chemical specificity as molecules contain spectral fingerprints due to distinct bond vibrations.⁹ IR microscopy provides high sensitivity due to the large absorption cross section of vibrational modes, but it is limited by low spatial resolution and strong water absorption.^{10,11} In contrast, Raman spectroscopy and microscopy have circumvented these limitations,^{12,13} offering chemical-specific detection and quantitative analysis of biological samples,¹⁴ and demonstrated

potential in clinical applications.^{15–17} Raman spectroscopy combined with endoscopic techniques has made breakthroughs in the diagnosis and treatment of early digestive tract tumors.^{18–20} However, the Raman effect is so weak that data acquisition usually takes too much time for practical imaging tasks.²¹

Stimulated Raman scattering (SRS) offers a gain of Raman scattering efficiency by 3–5 orders of magnitude, enabling high-speed chemical imaging.^{22–25} SRS microscopy hence overcomes the speed limit of Raman imaging while retaining the spectral identities for molecule-specific detection. Moreover, SRS microscopy could provide tissue histology similar to traditional H&E staining based on the chemical contrast of intrinsic biomolecules such as lipids, proteins, and DNA.^{25–30} Compared with frozen H&E staining, SRS microscopy has the advantages of imaging fresh, unprocessed tissues to achieve near real-time tissue histology in the operating room.^{31–33} In addition to lipid and protein contents, collagen fibers are known to correlate with cancer fibrosis and tumor cell intravasation^{34,35} and may play a protective role in controlling

pancreatic cancer progression.³⁶ Hence, it is necessary to include collagen fiber-specific detection with second harmonic generation (SHG) during SRS imaging.^{37–40} Up to now, SRS/SHG microscopy has shown potential in the diagnosis and evaluation of many types of human tumor tissues, including laryngeal carcinoma, brain tumor, and breast cancer.^{26,27,40–42} However, the possibility of use of SRS microscopy for human pancreatic tumor imaging and intraoperative guidance has never been investigated.

Here, we report the use of SRS/SHG microscopy to image pancreatic tissues in a label-free manner, demonstrating that key histological features could be revealed by SRS to yield similar diagnostic power as traditional H&E staining. Furthermore, we showed that pancreatic fistula could be evaluated by analyzing the content of collagen fibers. Our results demonstrated the potential of SRS microscopy for rapid intraoperative diagnosis and evaluation of pancreatic cancer.

■ EXPERIMENTAL SECTION

Sample Preparation. All tissue samples were collected from patients at the Huashan Hospital and approved by the Ethics Committee with informed written consent (KY2019001). Pancreatic tissues from surgical margins and tumors were resected during pancreatic surgery. To prevent autolysis, freshly excised tissues were quickly immersed in 5% formalin solution for slight fixation and stored at $-20\text{ }^{\circ}\text{C}$ for further tests. To correlate SRS with traditional H&E staining, tissues were sectioned using a fast cryotome (CM1950, Leica) into pairs of adjacent $10\text{ }\mu\text{m}$ - and $4\text{ }\mu\text{m}$ -thick slices. The $10\text{ }\mu\text{m}$ slices were used for SRS imaging directly without additional processing, and the $4\text{ }\mu\text{m}$ slices were sent for frozen H&E staining following standard procedures. For fresh tissue imaging, surgical tissues were sealed between two coverslips and a perforated glass slide ($\sim 0.5\text{ mm}$ thickness) and then imaged under an SRS microscope without further processing.

Setup of the SRS Microscope. The energy diagrams of the optical transitions are illustrated in Figure 1A. In spontaneous Raman scattering, the pump photons of frequency ω_p interact with bond vibrations to generate frequency-red-shifted Stokes photons of ω_s , whereas SRS requires the simultaneous interaction of both pump and Stokes photons with the sample. Stimulated amplification occurs when the difference frequency, $\Delta\omega = \omega_p - \omega_s$, matches a particular bond vibrational frequency Ω . The SHG process requires the selection of noncentrosymmetric structures, such as collagen fibers in biological tissues.

The details of the experimental apparatus of the SRS/SHG microscope are provided in our previous study.⁴⁰ For SRS imaging, a dual-output femtosecond optical parametric oscillator (OPO, InSight DS+, Newport) was used as the laser source. The Stokes beam was fixed at 1040 nm, and the pump beam was tunable within 690–1300 nm (802 nm was used in this study). Both beams were chirped to picoseconds using SF57 glass rods to work under the “spectral focusing” mode, where the detection Raman frequencies were selected by adjusting the time delay between the pump and Stokes pulses.³³ The combined beams were guided into a commercial laser scanning microscope (FV1200, Olympus) and focused onto samples through an objective lens (UPLSAPO 60XWIR, NA1.2 water). The optical power of the pump and Stokes beams at the sample was kept around 40 and 50 mW, respectively. The Stokes beam was modulated at 10 MHz, and the stimulated Raman loss signal of the pump beam was

demodulated using a lock-in amplifier (HF2LI, Zurich Instruments) to generate SRS images in the transmission mode. The SHG signal generated by the pump beam was filtered by a narrow bandpass filter (FF01-405/10-2S, Semrock) and simultaneously collected by a photomultiplier tube to yield SHG images in the epi mode.

Multichannel Image Processing. We applied the standard numerical decomposition algorithm to extract the lipid and protein contents from the raw SRS data containing images taken at 2845 and 2930 cm^{-1} ,^{26,40} based on the measured SRS spectra of each chemical composition. The SHG channel was used directly to represent the collagen fibers without further image processing. For large-scale tissue imaging, we used Olympus software (FluoView) for automated mosaic tiling and generated full-sized images by stitching each field of view with a custom-written MATLAB program.

Quantitative Analysis of Pancreatic Fibrosis. Fibrosis quantification and scoring using SHG imaging have been demonstrated in lung, kidney, and liver tissues.^{39,43–45} The SHG index, calculated from the surface density of binary distribution of the SHG signal above an optimal threshold, allows for the discrimination of fibrosis levels.⁴⁶ In this report, a correlation analysis between collagen fibrosis and pancreatic fistula was performed using ImageJ software to measure the area ratio of collagen fibers in each tissue slice. In particular, we first set appropriate thresholds of SRS (protein) and SHG (collagen fiber) channels and converted them to binary maps. Then, we measured the total pixel numbers of both the binarized SHG and SRS maps to quantify the areas of the collagen fiber and the overall tissue size, respectively. As a result, the area ratio of the collagen fiber within the whole tissue can be calculated to represent the fibrosis density for each pancreatic tissue.

Clinical Data Collection and Statistical Analysis.

Patient hospital charts, operative reports, and pathological diagnosis were reviewed. From these records, age, sex, type of procedure, and pancreatic amylase (PAMY) level from the peritoneal drainage on 5 ± 1 days after surgery were identified. Our main outcome measures about postoperative pancreatic fistula were the PAMY level. A statistical analysis was conducted using the Prism 5 GraphPad software program (GraphPad Software, Inc.) and shown as mean \pm standard error of mean. Data were analyzed using a two-tailed unpaired Student's *t*-test and Fisher's exact test. The results were considered significant if $p < 0.05$.

■ RESULTS AND DISCUSSION

Characterization of the SRS Microscope. We first measured the SRS spectra of oleic acid and bovine serum albumin to calibrate our microscope system and used them as the spectra of standard lipid and protein for a later chemical decomposition analysis (Figure S1). As can be seen, the lipid spectrum exhibits strong peaks at both the CH_2 (2845 cm^{-1}) and CH_3 (2930 cm^{-1}) vibrations, while the protein shows a strong CH_3 but minimal CH_2 signal. SRS spectra of the biological specimen indicate that the cell nucleus contains much less lipid and relatively more protein, whereas the cytoplasm yields more lipid features as seen in the higher CH_2 signal (Figure 1B). A typical pancreatic tissue imaging result is shown in Figure 1C, where the pancreatic islets show overall lipid-rich structures such as lipid droplets, while the cell nucleus appears more abundant in proteins. These features offer chemical contrast of tissue histology by decomposing the

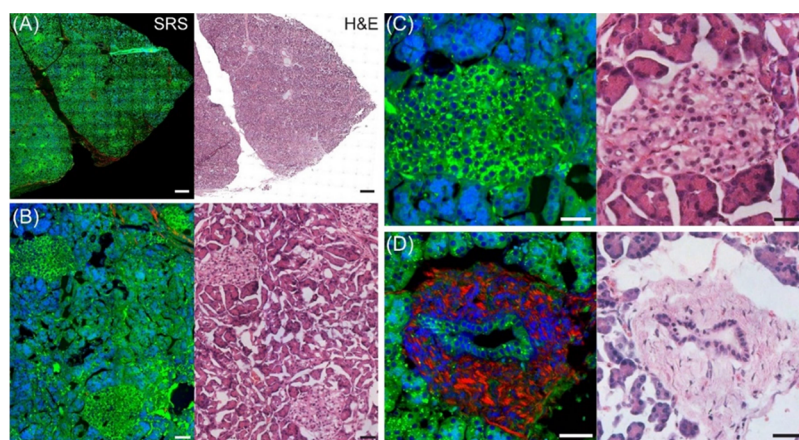


Figure 2. Imaging key histological features in normal pancreatic frozen tissue sections. Adjacent sister sections were imaged with SRS and H&E for comparison. (A) Whole tissue section. (B) Partially enlarged region with normal pancreatic islets and acini. (C) Magnified image of a typical pancreatic islet. (D) A typical normal pancreatic duct surrounded by dense collagen fibers (red). Scale bars: (A) 200 μm and (B–D) 50 μm .

raw SRS images taken at the two Raman frequencies into the distributions of lipid and protein. Furthermore, combined with the collagen fibers imaged with SHG, pancreatic tissues demonstrated well-resolved compositional profiles of lipid (green), protein (blue), and collagen fibers (red), forming three-color images with histological information for tissue diagnosis (Figure 1C).

Histological Features of Normal Pancreatic Tissues Revealed by SRS. We first imaged the normal pancreatic frozen tissue sections to evaluate the capability of SRS microscopy in revealing pancreatic histoarchitectures. SRS and H&E images of adjacent thin sections are shown in Figure 2, demonstrating the ability of SRS to image the most relevant tissue structures of pancreas, including the pancreatic islets, ducts, and acini. By comparing the two imaging modalities, label-free SRS could successfully provide almost identical histological information as H&E staining. The overall tissue histoarchitectures could be clearly visualized at large scales (Figure 2A,B), with high-resolution detailed structures shown in the zoomed-in images. Normal pancreatic islet features a high lipid content with regularly patterned islet cells (Figure 2C). The normal pancreatic duct characterizes the regularly shaped single-layer cell pattern with a typical polarized cellular morphology (Figure 2D). Interestingly, almost every pancreatic duct is found to be surrounded by a cluster of collagen fibers as revealed in the SHG channel. It can also be seen that most of the normal pancreatic tissues are filled with a large number of acinar cells, which have less lipids than the islets, and their nucleus could be well resolved by SRS (Figure 2C,D). Note that SRS may be able to reveal better tissue morphologies than frozen H&E staining since the latter is likely to experience morphological shifts during tissue preparations, such as freezing artifacts and cell shrinkage after dehydration (H&E in Figure 2C,D).

In addition to the above pancreatic-specific features, SRS is also capable of imaging other general tissue architectures in pancreas. For instance, intrapancreatic blood vessels could be readily seen (Figure 3, asterisks), which are distinctly different from the pancreatic ducts, lacking the single-layer cellular structure or the surrounding collagen fibers. Although rich in proteins, these small blood vessels do not show the SHG signal (mainly from type I collagen fibers). Moreover, myelinated nerves with abundant lipids and bundle structures could be

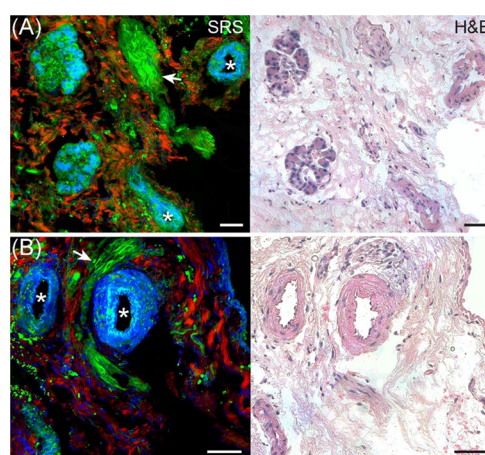


Figure 3. SRS histology of general features in chronic pancreatitis. (A) Cross sections of small blood vessels (asterisks), myelinated nerves (arrow heads), and acini and collagen fibers (red). (B) Another region. Scale bar: 50 μm .

clearly visualized (Figure 3, arrow heads). Regularly packed acinar cells could also be visualized in Figure 3A. Hence, we have shown that SRS microscopy could differentiate consistent histological features of normal pancreatic tissues with conventional H&E staining.

SRS Imaging of Different Types of Pancreatic Tumors. Next, we performed SRS imaging on pancreatic tumor tissue sections. The most common and malignant type of pancreatic tumor is the ductal adenocarcinoma of the pancreas. A typical tissue section of pancreatic ductal adenocarcinoma imaged with SRS is shown in Figure 4A, along with the H&E result on the adjacent section. Critical diagnostic features of ductal adenocarcinoma could be clearly visualized. The neoplastic pancreatic ducts show not only irregular ductal shapes (Figure 4B) but also cellular atypia, such as the loss of polarity, abnormal nucleus sizes and shapes, and conspicuous mitotic figures, whereas the pancreatic islet usually does not provide obvious diagnostic hallmarks in the ductal adenocarcinoma (Figure 4C). At the early stage of ductal adenocarcinoma, the pancreatic duct maintains roughly a regular shape, but the cells developed cellular atypia with abnormal arrangements (Figure 4D). In sharp contrast, the later stage of the disease demonstrated an obviously disrupted

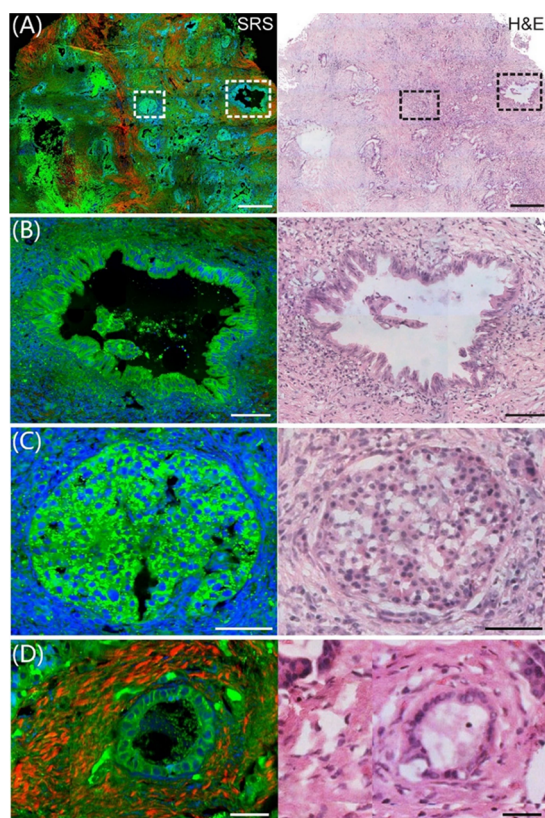


Figure 4. Microphotographs of SRS and H&E staining of key histological features in pancreatic ductal adenocarcinoma tissue sections. (A) Low magnification of the tissue section. (B) Moderately differentiated adenocarcinoma. (C) Enlarged view of the pancreatic islet. (D) Well-differentiated ductal adenocarcinoma. Scale bars: (A) 200 μm and (B–D) 40 μm .

ductal morphology (Figure 4B). From the combined SRS/SHG images, we realized that the abnormally developed collagen fibers might correlate with cancerous tissues (Figure 4A), in contrast to the normal tissues (Figure 2A). Note that SHG could provide more sensitive detection of collagen fibers than conventional H&E staining and will be used in quantitative analysis later in this study. Moreover, we applied SRS microscopy in imaging another type of pancreatic tumor: intraductal papillary mucinous neoplasm (IPMN) of the pancreas. As shown in Figure 5, IPMN is composed of mucin-producing columnar cells showing papillary proliferation and variable degrees of cellular atypia arising from the main pancreatic duct or its branches. Histological details of IPMN in the pancreatic duct could be readily seen from the SRS images, agreeing extremely well with the adjacent H&E images (Figure 5B,C).

Based on the capability of SRS in revealing key histological features of pancreatic tissues, we next evaluated the potential of SRS for intraoperative diagnosis of pancreatic cancer. Tissues from resection margins of 37 patients were harvested (Table S1), and each generated a pair of sister sections for SRS and frozen H&E, some of which are shown in Figure S2. Two experienced pathologists were given 37 pairs of randomly ordered SRS and H&E images to rate them based on their clinical knowledge. Pathologists were briefly trained on the principle and examples of SRS imaging, and their rating results were collected as “positive” or “negative” for the classification of tumor or normal (Table 1). The rating results were further

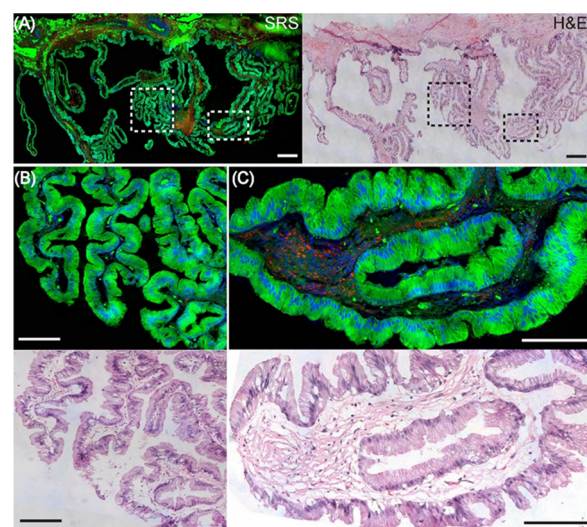


Figure 5. SRS imaging of IPMN of the pancreas. (A) Whole tissue section. (B,C) Enlarged view of the dashed boxes. Scale bar: 200 μm .

Table 1. Survey Results^a

diagnosis		P1		P2		accuracy (%)
		☑	☒	☑	☒	
+	H&E	2	0	2	0	100
	SRS	2	0	2	0	100
−	H&E	35	0	35	0	100
	SRS	34	1	35	0	97.14
total	H&E	37	0	37	0	100
	SRS	36	1	37	0	97.3
accuracy (%)		97.3		100		
concordance		97.3		100		

^a37 pairs of SRS and H&E images from adjacent frozen tissue sections from resection margins were evaluated by two pathologists (P1 and P2) in a random order. Each image was rated as “positive” (+) or “negative” (−) and compared with the standard histopathology.

compared with the pathological results from the hospital. The statistical analysis of pathologists’ diagnosis on SRS and frozen H&E images showed significant high concordance (Cohen’s kappa, $\kappa = 0.973-1$), indicating that SRS could provide similar diagnostic power as frozen H&E staining for pancreatic cancer.

Fresh Tissue Imaging with SRS. To simulate label-free intraoperative histology, we performed SRS imaging on fresh, unprocessed pancreatic tissues. Fresh tissue imaging is advantageous not only for its reduced time and cost but also for higher image quality of better-preserved tissue architectures without freezing or sectioning artifacts. As shown in Figure 6A, typical SRS images of fresh pancreatic tissues reveal all the important characteristic features as seen in frozen sections, including normal and cancerous pancreatic ducts (Figure 6B,C), acini (Figure 6D), and nerves (Figure 6E). Based on the results of both frozen sections and fresh tissues, we could conclude that SRS microscopy provides a potential rapid intraoperative tool for accurate evaluation of pancreatic tissue histology.

Correlation Analysis between Collagen Fibrosis and Pancreatic Fistula. In addition to the histological information, the spatial-chemical profiles in SRS/SHG images provide adequate data for quantitative analysis of biomolecular

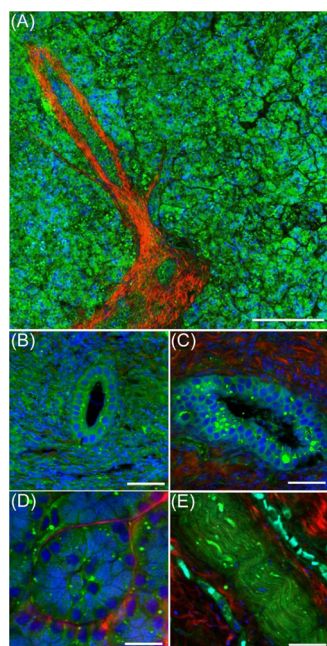


Figure 6. Imaging fresh pancreatic tissues. (A) Large-scale image. (B) Normal and (C) cancerous pancreatic ducts. (D) Acini and (E) nerve. Scale bars: (A) 200 μm and (B–E) 50 μm .

species.^{39,43,47} In particular, pancreatic fistula is related to reduced fibrosis and is hypothesized to correlate with the collagen fibers in pancreatic tissues. From our imaging results, we could indeed see large differences of collagen fibrosis between cases of pancreatic cancers. For instance, Figure 7A

shows a typical case with abundant collagen fibers and Figure 7B shows a case with far less collagen fibers. We quantified the area ratio of collagen fibers in the SRS/SHG image for each case and set 40% as the cutoff ratio and then correlated it with the PAMY level from the peritoneal drainage on 5 ± 1 days after surgery. Among the enrolled 30 patients, 15 patients had a <40% collagen fiber ratio, while 15 patients had a >40% ratio (Figure 7C). Remarkably, the PAMY level in lower collagen patients is significantly increased compared to higher collagen patients (3800 ± 960 vs 700 ± 450 U/L, $p = 0.0064$, Figure 7D). If we considered a PAMY level more than 1000 U/L as warning of poor prognosis (rebleeding, septic shock, reoperation, etc.), 66.7% patients with lower collagen had a >1000 U/L PAMY level, while 6.67% higher collagen patients had a >1000 U/L PAMY level (OR = 28.00; CI = 2.819–278.2; $p = 0.0017$, Figure 7E). The findings reveal the potential prediction value of intraoperative marginal collagen ratio quantified by SRS/SHG, which indicates early and aggressive intervention regimes for those patients.

CONCLUSIONS

The ideal R0 resection of pancreatic tumor surgery is to remove all local malignant tissues without any residual tumor cells left behind. In the clinic, evaluation of the resection margin requires a pathologist to examine the histopathology of several pieces of tissues harvested at the residual margin. Depending on the condition of the resected tissues, extended resection may be demanded to reach the goal of R0 resection for pancreatic tumor surgery. However, it is difficult to obtain real-time intraoperative assessment of tumor margins with traditional histology. Our current study and previous trials on

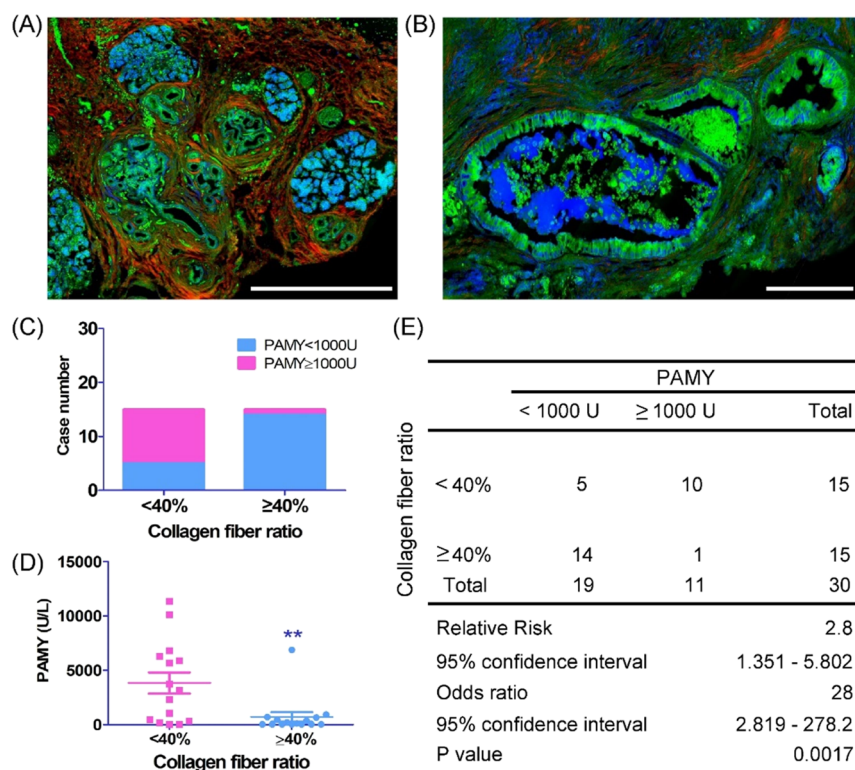


Figure 7. Evaluating pancreatic fistula with collagen fibrosis. Images of pancreatic tissues with (A) high and (B) low contents of collagen fibers. (C–E) Statistical analysis of the correlation between the PAMY level and the collagen ratio. $**p < 0.01$, compared to the collagen fiber ratio for the < 40% group. Scale bar: 500 μm .

various types of human tumor tissues have demonstrated the potential of SRS microscopy for rapid intraoperative histology on fresh tissues with a high diagnostic accuracy. Although the imaging depth of the current technology is limited (<200 μm), it is still possible to provide partial 3D histology, combining the intrinsic optical sectioning of SRS and physical resection during operations.^{26,48} Furthermore, taking advantage of the noninvasiveness of SRS, surgical tissues after imaging are still intact for further molecular and histological evaluations.

In our current study, most of the resection margins appear negative (35 among the total 37 cases), which limits the generalizability of the statistics. Nonetheless, the main diagnostic features of pancreatic ducts are so clear that the diagnostic accuracy remains high. With the rapid development of machine learning and artificial intelligence, image-based medical diagnosis has experienced vast advances in accuracy and efficiency.^{49,50} Deep learning algorithm-integrated SRS histology has also been developed by several research groups for the rapid diagnosis of human tumors, including brain tumor and laryngeal carcinoma.^{31,32,40} There is also need for deep learning-assisted SRS histology in diagnosing pancreatic tissues, but the strategy may be altered. Unlike brain tissues, pancreatic tissues appear much more heterogeneous, and the key diagnostic features are much more localized—mostly rely on the histoarchitecture of pancreatic ducts. Hence, different machine learning algorithms will be needed to emphasize the most relevant structures, and image segmentation could play an important role. In future studies, increased and balanced sizes of data sets among categories would be needed for training and testing appropriate neural networks.

Although the correlation study of pancreatic fistula and collagen fibrosis remains quite preliminary in the current study, it may potentially serve as a quantification method to evaluate the risk of pancreatic fistula. It is currently recognized that the prognostic factors related to pancreatic fistula include soft texture of the pancreas, small diameter of the pancreatic duct, high intraoperative blood loss (>400 mL), and high-risk pathological types. Hence, in addition to collagen fibrosis, histological measures may also be considered to enhance the prediction accuracy. For instance, the diameters of pancreatic ducts may be extracted from SRS images and added to the variables of evaluation algorithms.

In summary, we have demonstrated that coherent nonlinear microscopy could perform label-free histology for human pancreatic tissues. Key histological features could be readily visualized with SRS/SHG, yielding similar diagnostic results to traditional H&E staining. Moreover, quantitative analysis of SRS/SHG images revealed the correlation between collagen fibrosis and pancreatic fistula. Our study has broadened the potential applications of SRS microscopy for rapid intraoperative histology and quantitative fibrosis analysis, and the method may be extended to other types of solid tumors.

■ ASSOCIATED CONTENT

Supporting Information

The Supporting Information is available free of charge at <https://pubs.acs.org/doi/10.1021/acs.analchem.1c03861>.

Supplementary figures and table; patient information; SRS and spontaneous Raman spectra of standard chemicals; and typical SRS and H&E images used for the survey (PDF)

■ AUTHOR INFORMATION

Corresponding Authors

Lie Yao – Department of Pancreatic Surgery, Department of Neurosurgery, Department of Pathology, Huashan Hospital, Fudan University, Shanghai 200040, China;
Email: yaolie_sh@163.com

Minbiao Ji – State Key Laboratory of Surface Physics and Department of Physics, Human Phenome Institute, Academy for Engineering and Technology, Key Laboratory of Micro and Nano Photonic Structures (Ministry of Education), Fudan University, Shanghai 200433, China; Yiwu Research Institute of Fudan University, Yiwu City, Zhejiang 322000, China; orcid.org/0000-0002-9066-4008;
Email: minbiaoj@fudan.edu.cn

Authors

Lili Zhang – State Key Laboratory of Surface Physics and Department of Physics, Human Phenome Institute, Academy for Engineering and Technology, Key Laboratory of Micro and Nano Photonic Structures (Ministry of Education), Fudan University, Shanghai 200433, China; Present Address: State Key Laboratory of Infrared Physics, Shanghai Institute of Technical Physics, Chinese Academy of Sciences, Shanghai 200083, China

Xiang Zou – Department of Pancreatic Surgery, Department of Neurosurgery, Department of Pathology, Huashan Hospital, Fudan University, Shanghai 200040, China

Jing Huang – State Key Laboratory of Surface Physics and Department of Physics, Human Phenome Institute, Academy for Engineering and Technology, Key Laboratory of Micro and Nano Photonic Structures (Ministry of Education), Fudan University, Shanghai 200433, China

Jie Fan – Department of Pancreatic Surgery, Department of Neurosurgery, Department of Pathology, Huashan Hospital, Fudan University, Shanghai 200040, China

Xiangjie Sun – Department of Pathology, Fudan University Shanghai Cancer Center, Shanghai 200032, China

Bohan Zhang – State Key Laboratory of Surface Physics and Department of Physics, Human Phenome Institute, Academy for Engineering and Technology, Key Laboratory of Micro and Nano Photonic Structures (Ministry of Education), Fudan University, Shanghai 200433, China

Bin Zheng – Department of Otolaryngology, Zhejiang Provincial People's Hospital, People's Hospital of Hangzhou Medical College, Hangzhou 310014, China

Chongyuan Guo – Shanghai Starriver Bilingual School, Shanghai 201108, China

Deliang Fu – Department of Pancreatic Surgery, Department of Neurosurgery, Department of Pathology, Huashan Hospital, Fudan University, Shanghai 200040, China

Complete contact information is available at:

<https://pubs.acs.org/doi/10.1021/acs.analchem.1c03861>

Author Contributions

[○]L.Z., X.Z., and J.H. contributed equally.

Notes

The authors declare no competing financial interest.

■ ACKNOWLEDGMENTS

We acknowledge financial support from the National Natural Science Foundation of China (61975033 and 81970418), the Shanghai Municipal Science and Technology Major Project

(No. 2018SHZDZX01) and ZJLab, the Science and Technology Commission of Shanghai Municipality (Grant No. 18JC1410403), the MOE Frontiers Center for Brain Science, the Medicine and Health Research Foundation of Zhejiang Province (2019RC006), and the Zhejiang Provincial Natural Science Foundation of China (LY20H130005).

ABBREVIATIONS

SRS	stimulated Raman scattering
SHG	second harmonic generation
H&E	hematoxylin and eosin
PAMY	pancreatic amylase
IPMN	intraductal papillary mucinous neoplasm
OPO	optical parametric oscillator
SEM	standard error of mean
PMT	photomultiplier
ML	machine learning
FOV	field of view
OA	oleic acid
BSA	bovine serum albumin

REFERENCES

- (1) Howlader, N.; Noone, A. M.; Krapcho, M.; Miller, D.; Brest, A.; Yu, M.; Ruhl, J.; Tatalovich, Z.; Mariotto, A.; Lewis, D. R.; et al. *SEER Cancer Statistics Review, 1975–2017*; National Cancer Institute, 2020.
- (2) Bolm, L.; Mueller, K.; May, K.; Sondermann, S.; Petrova, E.; Lapshyn, H.; Honselmann, K. C.; Bausch, D.; Zemskov, S.; Bronsert, P.; et al. *Cancers* **2020**, *12*, 882.
- (3) Schlitter, A. M.; Esposito, I. *Cancers* **2010**, *2*, 2001–2010.
- (4) Bassi, C.; Marchegiani, G.; Dervenis, C.; Sarr, M.; Abu Hilal, M.; Adham, M.; Allen, P.; Andersson, R.; Asbun, H. J.; Besselink, M. G.; et al. *Surgery* **2017**, *161*, 584–591.
- (5) Roberts, K. J.; Hodson, J.; Mehrzad, H.; Marudanayagam, R.; Sutcliffe, R. P.; Muiesan, P.; Isaac, J.; Bramhall, S. R.; Mirza, D. F. *HPB* **2014**, *16*, 620–628.
- (6) Mathur, A.; Pitt, H. A.; Marine, M.; Saxena, R.; Schmidt, C. M.; Howard, T. J.; Nakeeb, A.; Zyromski, N. J.; Lillemo, K. D. *Ann. Surg.* **2007**, *246*, 1058–1064.
- (7) Yang, Y. *Chin. J. Gen. Surg.* **2016**, *25*, 1231–1235.
- (8) Zipfel, W. R.; Williams, R. M.; Christie, R.; Nikitin, A. Y.; Hyman, B. T.; Webb, W. W. *Proc. Natl. Acad. Sci. U. S. A.* **2003**, *100*, 7075–7080.
- (9) Evans, C. L.; Xie, X. S. *Annu. Rev. Anal. Chem.* **2008**, *1*, 883–909.
- (10) Miller, L. M.; Smith, G. D.; Carr, G. L. *J. Biol. Phys.* **2003**, *29*, 219–230.
- (11) Bhargava, R. *Appl. Spectrosc.* **2012**, *66*, 1091–1120.
- (12) Azemtsop Matanfack, G.; Ruger, J.; Stiebing, C.; Schmitt, M.; Popp, J. *J. Biophotonics* **2020**, *13*, No. e202000129.
- (13) Vlasov, A. V.; Maliar, N. L.; Bazhenov, S. V.; Nikelshparg, E. I.; Brazhe, N. A.; Vlasova, A. D.; Osipov, S. D.; Sudarev, V. V.; Ryzhykau, Y. L.; Bogorodskiy, A. O.; et al. *Crystals* **2020**, *10*, 38.
- (14) Jones, R. R.; Hooper, D. C.; Zhang, L. W.; Wolverson, D.; Valev, V. K. *Nanoscale Res. Lett.* **2019**, *14*, 231.
- (15) Berger, A. J.; Itzkan, I.; Feld, M. S. *Spectrochim. Acta A* **1997**, *53*, 287–292.
- (16) Huang, Z. W.; McWilliams, A.; Lui, H.; McLean, D. I.; Lam, S.; Zeng, H. S. *Int. J. Cancer* **2003**, *107*, 1047–1052.
- (17) Nijssen, A.; Schut, T. C. B.; Heule, F.; Caspers, P. J.; Hayes, D. P.; Neumann, M. H. A.; Puppels, G. J. *J. Invest. Dermatol.* **2002**, *119*, 64–69.
- (18) Coda, S.; Siersema, P. D.; Stamp, G. W. H.; Thillainayagam, A. V. *Endosc. Int. Open* **2015**, *03*, E380–E392.
- (19) Xu, Z. H.; Huang, W.; Lin, D.; Ge, X. S.; Lin, X. L.; Feng, S. Y.; Li, Y. Z.; Chen, R. *Spectrosc. Spect. Anal.* **2016**, *36*, 2518–2521.
- (20) Santos, I. P.; Barroso, E. M.; Schut, T. C. B.; Caspers, P. J.; van Lanschot, C. G. F.; Choi, D. H.; van der Kamp, M. F.; Smits, R. W. H.; van Doorn, R.; Verdijk, R. M.; et al. *Analyst* **2017**, *142*, 3025–3047.
- (21) van Manen, H. J.; Kraan, Y. M.; Roos, D.; Otto, C. *Proc. Natl. Acad. Sci. U. S. A.* **2005**, *102*, 10159–10164.
- (22) Freudiger, C. W.; Min, W.; Saar, B. G.; Lu, S.; Holtom, G. R.; He, C.; Tsai, J. C.; Kang, J. X.; Xie, X. S. *Science* **2008**, *322*, 1857–1861.
- (23) Cheng, J.-X.; Xie, X. S. *Science* **2015**, *350*, No. aaa8870.
- (24) Ao, J.; Fang, X.; Miao, X.; Ling, J.; Kang, H.; Park, S.; Wu, C.; Ji, M. *Nat. Commun.* **2021**, *12*, 3089.
- (25) Hu, F.; Shi, L.; Min, W. *Nat. Methods* **2019**, *16*, 830–842.
- (26) Ji, M.; Orringer, D. A.; Freudiger, C. W.; Ramkissoon, S.; Liu, X.; Lau, D.; Golby, A. J.; Norton, I.; Hayashi, M.; Agar, N. Y. R.; Young, G. S.; et al. *Sci. Transl. Med.* **2013**, *5*, No. 201ra119.
- (27) Ji, M.; Lewis, S.; Camelo-Piragua, S.; Ramkissoon, S. H.; Snuderl, M.; Venneti, S.; Fisher-Hubbard, A.; Garrard, M.; Fu, D.; Wang, A. C.; et al. *Sci. Transl. Med.* **2015**, *7*, No. 309ra163.
- (28) Lu, F.-K.; Basu, S.; Igras, V.; Hoang, M. P.; Ji, M.; Fu, D.; Holtom, G. R.; Neel, V. A.; Freudiger, C. W.; Fisher, D. E.; Xie, X. S. *Proc. Natl. Acad. Sci. U. S. A.* **2015**, *112*, 11624–11629.
- (29) Zhang, B.; Xu, H.; Chen, J.; Zhu, X.; Xue, Y.; Yang, Y.; Ao, J.; Hua, Y.; Ji, M. *Theranostics* **2021**, *11*, 3074–3088.
- (30) Ji, M.; Arbel, M.; Zhang, L.; Freudiger, C. W.; Hou, S. S.; Lin, D.; Yang, X.; Bacskai, B. J.; Xie, X. S. *Sci. Adv.* **2018**, *4*, No. eaat7715.
- (31) Orringer, D. A.; Pandian, B.; Niknafs, Y. S.; Hollon, T. C.; Boyle, J.; Lewis, S.; Garrard, M.; Hervey-Jumper, S. L.; Garton, H. J. L.; Maher, C. O.; et al. *Nat. Biomed. Eng.* **2017**, *1*, No. 0027.
- (32) Hollon, T. C.; Pandian, B.; Adapa, A. R.; Urias, E.; Save, A. V.; Khalsa, S. S. S.; Eichberg, D. G.; D'Amico, R. S.; Farooq, Z. U.; Lewis, S.; et al. *Nat. Med.* **2020**, *26*, 52–58.
- (33) He, R.; Xu, Y.; Zhang, L.; Ma, S.; Wang, X.; Ye, D.; Ji, M. *Optica* **2017**, *4*, 44–47.
- (34) Xu, S. S.; Xu, H. X.; Wang, W. Q.; Li, S.; Li, H.; Li, T. J.; Zhang, W. H.; Yu, X. J.; Liu, L. *J. Transl. Med.* **2019**, *17*, 309.
- (35) Han, W. J.; Chen, S. H.; Yuan, W.; Fan, Q. H.; Tian, J. X.; Wang, X. C.; Chen, L. Q.; Zhang, X. X.; Wei, W. L.; Liu, R. C.; Qu, J. L.; Jiao, Y.; Austin, R. H.; Liu, L. Y. *Proc. Natl. Acad. Sci. U. S. A.* **2016**, *113*, 11208–11213.
- (36) Chen, Y.; Kim, J.; Yang, S.; Wang, H.; Wu, C.-J.; Sugimoto, H.; LeBleu, V. S.; Kalluri, R. *Cancer Cell* **2021**, *39*, 548–565.
- (37) Ricard-Blum, S.; Baffet, G.; Theret, N. *Matrix Biol.* **2018**, *68–69*, 122–149.
- (38) Streets, A. M.; Li, A.; Chen, T.; Huang, Y. *Anal. Chem.* **2014**, *86*, 8506–8513.
- (39) Sun, W. X.; Chang, S.; Tai, D. C. S.; Tan, N.; Xiao, G. F.; Tang, H. H.; Yu, H. J. *Biomed. Opt.* **2008**, *13*, No. 064010.
- (40) Zhang, L.; Wu, Y.; Zheng, B.; Su, L.; Chen, Y.; Ma, S.; Hu, Q.; Zou, X.; Yao, L.; Yang, Y.; Chen, L.; Mao, Y.; Chen, Y.; Ji, M. *Theranostics* **2019**, *9*, 2541–2554.
- (41) Lu, F. K.; Calligaris, D.; Olubiya, O. I.; Norton, I.; Yang, W. L.; Santagata, S.; Xie, X. S.; Golby, A. J.; Agar, N. Y. R. *Cancer Res.* **2016**, *76*, 3451–3462.
- (42) Yang, Y.; Chen, L.; Ji, M. *J. Innovative Opt. Health Sci.* **2017**, *10*, No. 1730010.
- (43) Strupler, M.; Pena, A. M.; Ernest, M.; Tharaux, P. L.; Martin, J. L.; Beaupaire, E.; Schanne-Klein, M. C. *Opt. Express* **2007**, *15*, 4054–4065.
- (44) Pena, A. M.; Fagot, D.; Olive, C.; Michelet, J. F.; Galey, J. B.; Leroy, F.; Beaupaire, E.; Martin, J. L.; Colonna, A.; Schanne-Klein, M. C. *J. Biomed. Opt.* **2010**, *15*, No. 056018.
- (45) Tai, D. C. S.; Tan, N.; Xu, S.; Kang, C. H.; Chia, S. M.; Cheng, C. L.; Wee, A.; Wei, C. L.; Raja, A. M.; Xiao, G. F.; et al. *J. Biomed. Opt.* **2009**, *14*, No. 044013.
- (46) Gailhouste, L.; Le Grand, Y.; Odin, C.; Guyader, D.; Turlin, B.; Ezan, F.; Desille, Y.; Guilbert, T.; Bessard, A.; Fremin, C.; et al. *J. Hepatol.* **2010**, *52*, 398–406.
- (47) Wang, M. C.; Min, W.; Freudiger, C. W.; Ruvkun, G.; Xie, X. S. *Nat. Methods* **2011**, *8*, 135–U52.

(48) Ao, J. P.; Feng, Y. Q.; Wu, S. M.; Wang, T.; Ling, J. W.; Zhang, L. W.; Ji, M. B. *Small Methods* **2020**, *4*, No. 1900600.

(49) Gulshan, V.; Peng, L.; Coram, M.; Stumpe, M. C.; Wu, D.; Narayanaswamy, A.; Venugopalan, S.; Widner, K.; Madams, T.; Cuadros, J.; et al. *JAMA, J. Am. Med. Assoc.* **2016**, *316*, 2402–2410.

(50) Esteva, A.; Kuprel, B.; Novoa, R. A.; Ko, J.; Swetter, S. M.; Blau, H. M.; Thrun, S. *Nature* **2017**, *542*, 115–118.